

<sub>1</sub> Preliminary design studies of a drift tube detector for  
<sub>2</sub> SHiP experiment

<sub>3</sub> Bereziuk Ivan

<sub>4</sub> September 15, 2015

## 5    1 Introduction

6   <sup>1</sup> The completion of the particle content of the Standard Model (SM) with the discovery of the  
7    Higgs boson, and advances in cosmology highlight the necessity for a new level of understanding  
8    of physics Beyond the Standard Model (BSM). At the same time, neither experiment nor theory  
9    provide clear hints of the nature or the scale of this new physics.

10    Over the next decades the Fermi-mass scale, and even beyond, will be comprehensively  
11    explored either directly by ATLAS and CMS at the LHC, or indirectly, assuming generic  
12    couplings, at experiments like LHCb, Belle2 and NA62 [1]. Hidden particles, which interact very  
13    weakly with the SM particles, are predicted in many theoretical models capable of explaining the  
14    shortcomings of the SM. A large part of their accessible parameter space remains unexplored.

15    In this situation SHiP is a recently proposed new general purpose fixed target facility at  
16    the SPS which is aimed at exploring the domain of hidden particles and make measurements  
17    with tau neutrinos. Hidden particles are predicted by a large number of models beyond the  
18    Standard Model. The high intensity of the SPS 400 GeV beam allows probing a wide variety  
19    of models containing light long-lived exotic particles with masses below  $10 \text{ GeV}/c^2$ , including  
20    very weakly interacting low-energy SUSY states.

### 21    1.1 Overview of the Experiment

22    At the energy accessible at the SPS, the hidden particles are predominantly produced in decays  
23    of hadrons, in particular in decays of charmed and beauty hadrons above the kaon mass, and  
24    in proton bremsstrahlung.

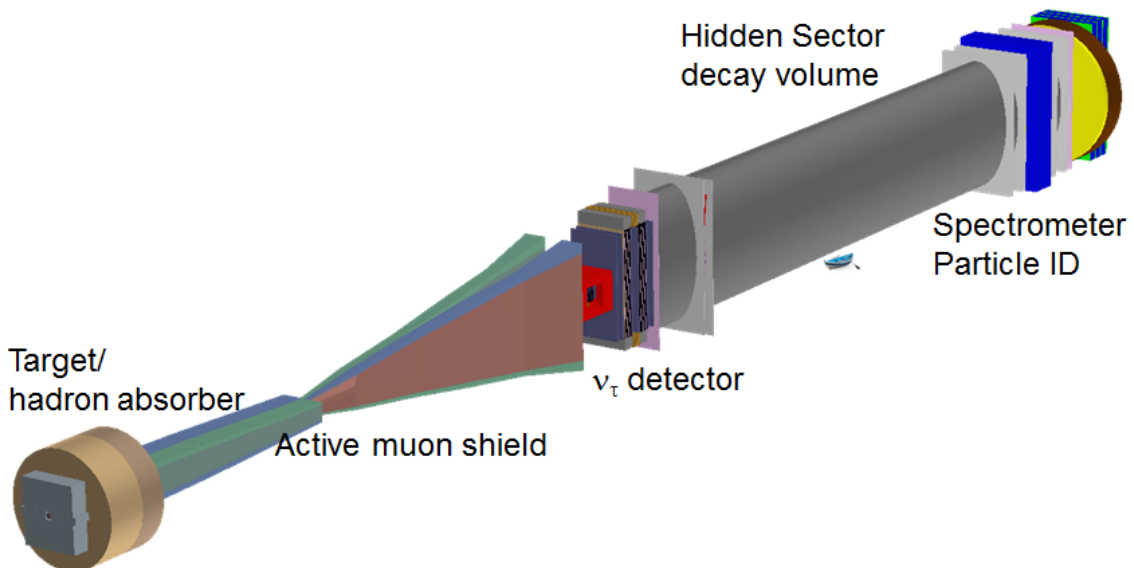


Figure 1: Overview of the SHiP facility [2]

---

<sup>1</sup>This section mostly(The information of for this section was) taken from SHiP Technical Proposal (TP) document [2] just to overview the experiment and prepare reader for subsequent work under separate part of detector.

25      The detector for the direct detection of the hidden particles is designed to fully reconstruct  
 26    their exclusive decays. Table 1 summarizes the main decay modes of the hidden particles in  
 27    the various models considered.

Table 1: Summary of the main decay modes of hidden particles in various models ( $\ell = e, \mu$ ).

| Models   | Final states   |
|--|--|
| Neutrino portal, SUSY neutralino               | $\ell^\pm\pi^\mp, \ell^\pm K^\mp, \ell^\pm\rho^\mp, \rho^\pm \rightarrow \pi^\pm\pi^0$ |
| Vector, scalar, axion portals, SUSY sgoldstino | $\ell^+\ell^-$   |
| Vector, scalar, axion portals, SUSY sgoldstino | $\pi^+\pi^-, K^+K^-$   |
| Neutrino portal ,SUSY neutralino, axino        | $\ell^+\ell^-\nu$  |
| Axion portal, SUSY sgoldstino                  | $\gamma\gamma$   |
| SUSY sgoldstino                                | $\pi^0\pi^0$   |

28      The principal background to the hidden particle decay signal originates from the inelastic  
 29    scattering of neutrinos and muons in the vicinity of the detector producing long-lived particles.

30      The beam line is designed to minimize the background sources. The proton interaction in  
 31    the target gives rise to a copious direct production of short-lived resonances, pions and kaons.  
 32    While a hadron stopper of a few metres of iron is sufficient to absorb the hadrons and the  
 33    electromagnetic radiation emerging from the target, the decays of pions, kaons and short-lived  
 34    resonances result in a large flux of muons and neutrinos. In order to reduce the flux of neutrinos,  
 35    in particular the flux of muon neutrinos and the associated muons, the pions and kaons should  
 36    be stopped as efficiently as possible before they decay. The target must therefore be made of  
 37    a material with the shortest possible interaction length and be sufficiently long to contain the  
 38    hadronic showers with minimum leakage. Since the production angle of the hidden particles is  
 39    relatively large, there is no requirement to minimize the beam spot.

40      The short-lived resonances and the residual flux of decaying pions and kaons still give rise to  
 41    a large flux of muons. This flux must be efficiently cleared from the detector fiducial volume by  
 42    either a passive shield or through an active shield based on magnetic deflection. The residual  
 43    flux should also be low enough so not to compromise the occupancy limit in the tau neutrino  
 44    detector. As illustrated in Figure 1, in the baseline design a 5 m horizontally wide region  
 45    respecting these requirements has been achieved with a 48 m long active muon shield based on  
 46    magnetic deflection of the muons in the horizontal plane.

47      The muon shield is followed by the 10 m long tau neutrino detector, which puts the start of  
 48    the HS decay volume at about 64 m [2]. The main purpose of the tau neutrino detector is to  
 49    perform the first direct observation of the  $\bar{\nu}_\tau$ , and to study the properties and the cross section  
 50    of  $\nu^\tau$  and  $\bar{\nu}_\tau$ . The current optimization of muon shield and cost, results in a decay volume with  
 51    an elliptical shape of 5 m width and 10 m height. The length of the decay volume is obtained  
 52    by maximizing the acceptance to the hidden particle decay products given the transversal size.

53      The full reconstruction of the hidden particle decays requires a magnetic spectrometer and  
 54    a system for particle identification at the end of the decay volume.

55      The particle identification system requires an electromagnetic calorimeter for  $e/\gamma$  identifica-  
 56    tion with sufficient granularity and energy resolution in order to reconstruct  $\pi^0$ 's, and a hadron  
 57    calorimeter in combination with a muon detector for  $\pi/\mu$  separation.

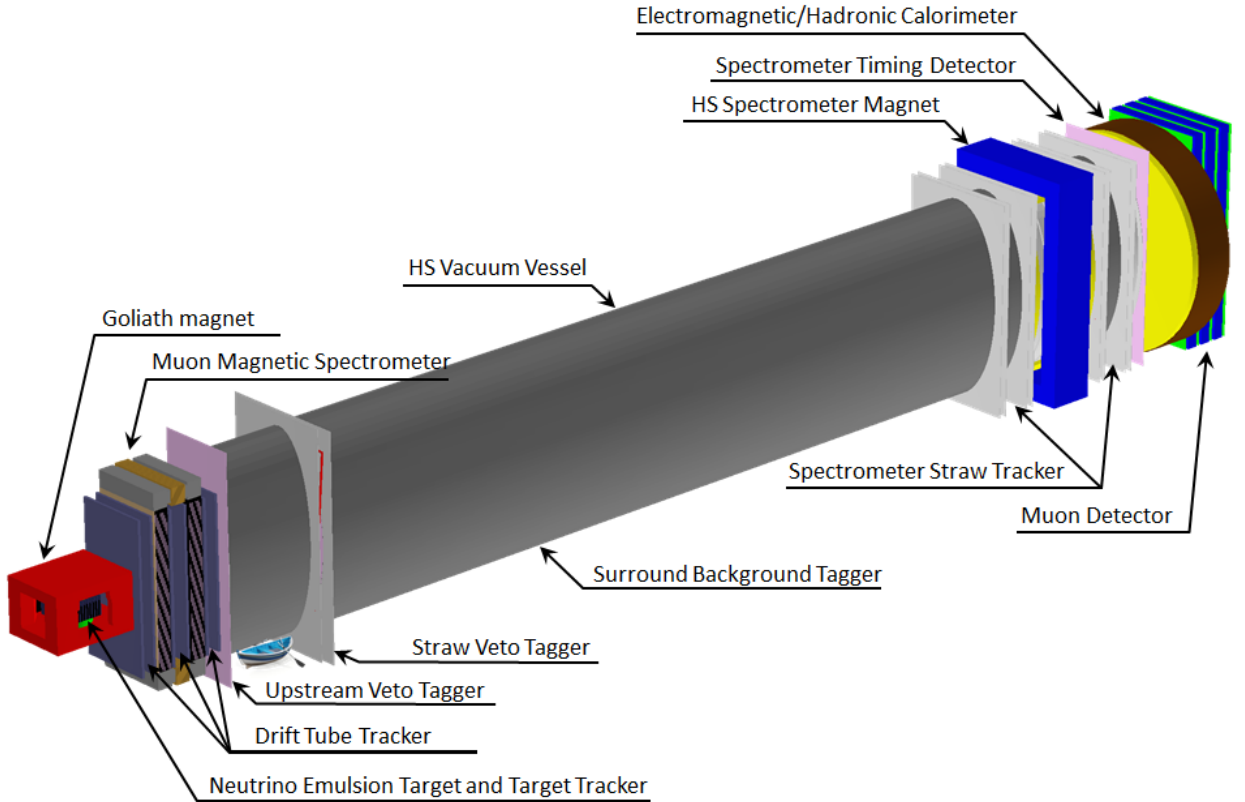


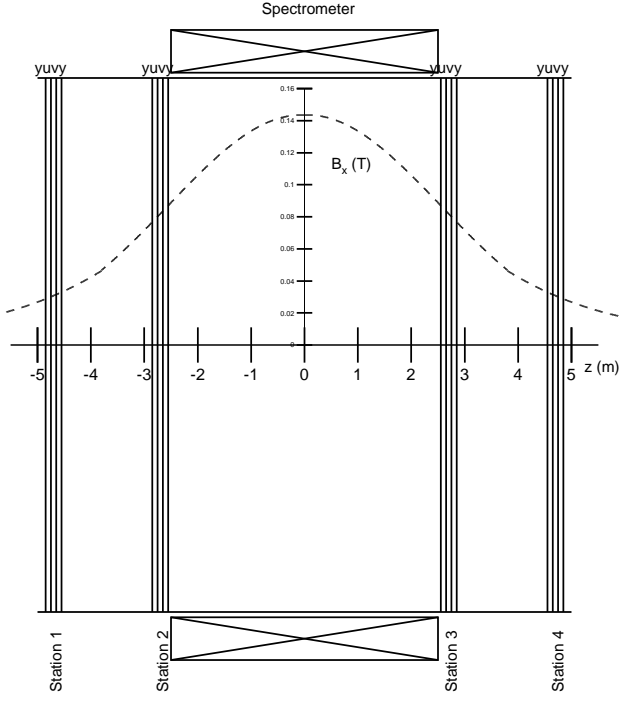
Figure 2: SHiP detector layout

## 58 1.2 Spectrometer tracker

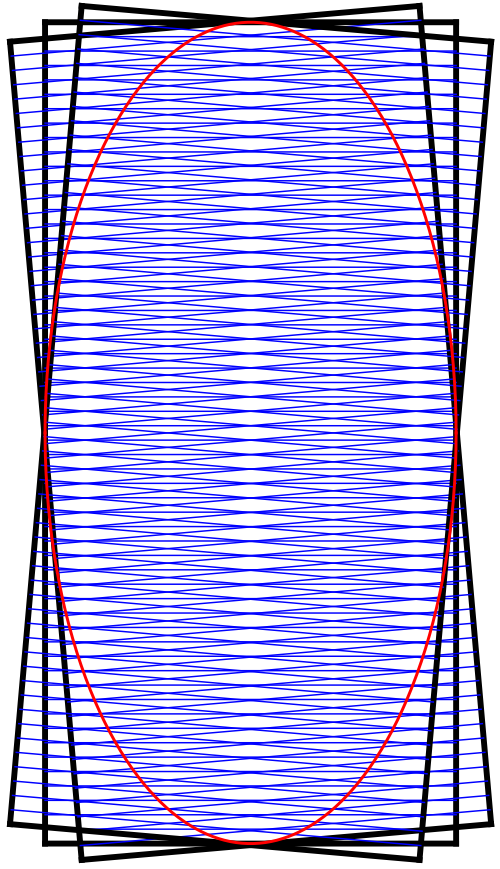
59 Spectrometer tracker is a part of particle identification system. The purpose of the HS spec-  
 60 trometer is to reconstruct with high efficiency the tracks of charged particles from the decay  
 61 of hidden particles. The spectrometer must provide an accurate determination of the track  
 62 momentum and of the flight direction within the fiducial decay volume.

63 The spectrometer consists of a large aperture dipole magnet and two tracking telescopes on  
 64 each side of the magnet. A layout with four tracking stations symmetrically arranged around  
 65 the dipole magnet, as depicted in Figure 3a, is taken as a baseline. The size and layout of the  
 66 tracker stations is connected to the size of the magnet. A dipole spectrometer magnet with a  
 67 horizontal gap of 5 m, a height of 10 m and a length of 5 m provides good acceptance coverage  
 68 and is considered feasible at a reasonable cost.

69 Following the direction of the magnetic field, the measuring elements are oriented horizon-  
 70 tally to measure precisely the vertical (Y) coordinate. Two stereo views (U and V) are rotated  
 71 by an angle  $\pm\theta_{stereo}$  for measuring the transverse coordinate X with an accuracy degraded by  
 72  $\sim 1/\sin\theta_{stereo}$ . The precision in X (i.e. the value of the stereo angle) is driven by the need  
 73 of a good enough measurement of the decay vertex, opening angle of the daughter particles  
 74 (which enters the invariant mass) and impact parameter at the production target. Each station  
 75 contains 4 views (Y-U-V-Y). The two stations on the same side of the magnet are separated by  
 76  $\Delta = 2m$  and a gap of 5m is left between the second and third stations (i.e. each is 2.5m away  
 77 from the centre of the magnet).



(a) Position of the tracking stations and dipole magnet, overlaid with magnetic field component  $B_x$  as a function of  $z$ .



(b) Four views in one station (not all straws shown, for the sake of clarity). The nominal acceptance, defined by the vacuum vessel, is shown as a red ellipse.

Figure 3: Spectrometer layout

The tracking stations of the magnetic spectrometer must provide good spatial resolution and minimise the contribution from multiple scattering. In addition, the tracker must operate in vacuum. A straw tracker made of thin polyethylene terephthalate (PET) tubes is ideal to meet these goals. Gas tightness of these tubes has been demonstrated in long term tests and the mass production procedure is also well established (see NA62 experiment [1]). The main differences between the SHiP tracker and the NA62 tracker are the need for 5 m long straws (vs 2.1 m in NA62). The main changes with respect to the Expression of Interest [6] follow from the changes applied to the spectrometer magnet. The straw orientation has been turned from vertical to horizontal and one transverse dimension has been increased from 5 to 10 m.

## 2 Subject of study

With new requirements for new straw tracker we have important challenge for long straws. It is related with the fact that straw and wire will be subjected to gravitational and electrical

90 forces and it causes the sagging. Because the straws are oriented horizontally (or almost, in  
91 case of stereo views), sagging is expected to cause in most drift tubes a downward deflection,  
92 which might be exploited when applying a correction.

93 Undoubtedly the presence of sagging can complicate the data processing stage and somewhat  
94 worse accuracy of track reconstruction. Primary question we have to investigate "is acceptable  
95 sag-admitting design?" and "What a downgrade of precision for sag-admitting design?".

96 Results of measurements on prototypes are discussed in Section 8.

### 97 3 Signal

98 Computer program Garfield [3] is designed for detailed simulation of two- and three-dimensional  
99 gas detectors. So we will perform STRAW tube studies using this program.

100 Charged particle create electron-ion pairs while traverse the drift tube. Electrons under  
101 affecting the electric field drift to the wire anode (see Fig.4). During the travel they increase  
102 their energy and invoke an avalanche. Therefore they produce a measurable signal.

103 Initial electrons drift to the wire due to the electrical field between the wire and the tube  
104 wall. Electrons ionize gas molecules due to the high electric field around the wire, especially  
105 near the wire when the strength of the electric field becomes very large. Subsequently readout  
106 electronics process the signal induced on the wire.

107 The event is registered if signal reach some a threshold voltage (Fig. 5). So the value of  
108 threshold is a key factor on the way of searching optimal setting for signal processing procedure.

Table 2: STRAW tube parameters

| parameter name           | value                           |
|--------------------------|---------------------------------|
| wire                     | $30 \mu m$ gold-plated Tungsten |
| straw length             | 5 m                             |
| voltage                  | 1750 V                          |
| inner tube radius        | 9.8 mm                          |
| wire medium density      | $19.3 g/cm^3$                   |
| wire tension             | $\sim 90 g$                     |
| working tube gas mixture | Ar 70% $CO_2$ 30%               |

109 We have to set threshold as low as possible but enough above from noise level to achieve  
110 best rate of true/false detected tracks and highest track registration precision and efficiency.

111 A variation of the signal height introduces a variation in the time when the signal passes  
112 the threshold and is considered to be the main contribution to the STRAW tracker resolution.

113 In the track reconstruction software(GARFIELD [3]) an effective TR-relation is used. It only  
114 describes the relation between the drift time and the distance from the track to the wire, which  
115 differs from the distance to the ionization cluster. The shape of the TR-relation is defined by  
116 the drift velocity of the ionization cluster inside the straw. The electric field increases towards  
117 the wire, leading to a non linear TR-relation.

118 The drift time versus the unbiased distance distribution and the result of the fit are shown  
119 in Fig. 17a. Noise hits under the main distribution, i.e. at earlier times, are due to primary  
120 or secondary particles ( $\delta$ -rays) passing the straw at a closer distance to the wire, consequently

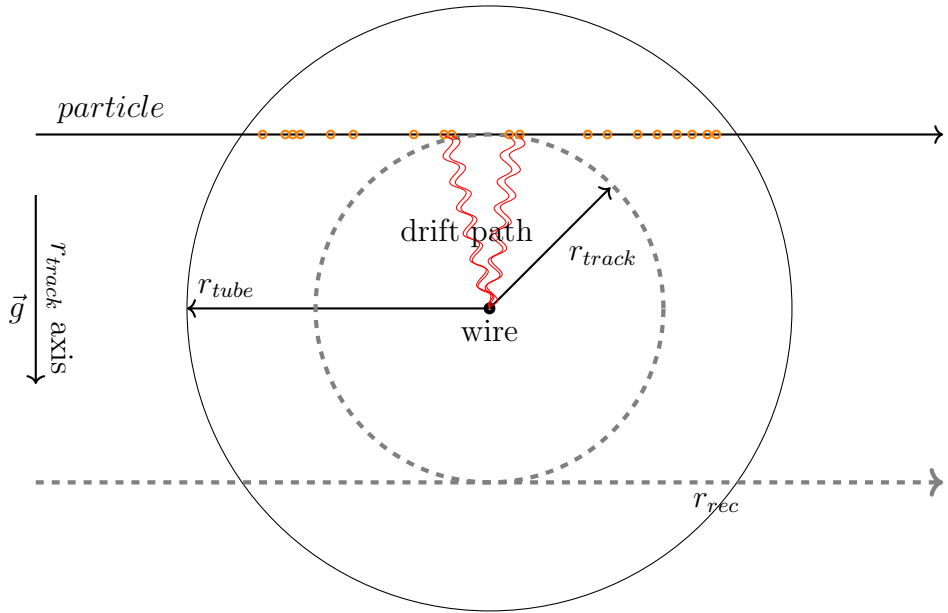


Figure 4: Schematic view of a particle passing the straw and producing ionization clusters (orange points). Electrons of ionization cluster drift to the wire and induce the signal. The closest distance from the track to the wire,  $r_{track}$ , and radius of the straw,  $r_{tube} = 2.45\text{mm}$ , are also indicated.

<sup>121</sup> producing an earlier signal. Initial clusters along the track are marked by orange points in the  
<sup>122</sup> figure.

<sup>123</sup> Muon  $\mu$  was chosen as test particle for simulation with energy  $1\text{GeV}$ . You can see some of  
<sup>124</sup> typical tracks from the  $\mu$  through the tube Fig.10a,10b.

### <sup>125</sup> 3.1 Leakage noise

<sup>126</sup> Every time we deal with different kind of noise. Basically it is noise from leakage current  
<sup>127</sup> through readout electronics.

<sup>128</sup> As will be discussed further we analyse not the current invoked by particle but the output  
<sup>129</sup> voltage from amplifier. In GARFIELD we able convolute input current  $I(t)$  with electronic  
<sup>130</sup> response function (1)<sup>2</sup>

$$f_{resp} = A \cdot (e^{-t/0.005} - e^{-t/0.030}) \quad (1)$$

<sup>131</sup> Noise is very important for every calculations and it makes bit impact on straw precision  
<sup>132</sup> and straw efficiency. So we can't rely on results until we receive signal and noise from real  
<sup>133</sup> STRAW tube prototypes.

<sup>134</sup> Convolution of input current makes it smooth. Usually in typical conditions<sup>3</sup> noise have  
<sup>135</sup> gauss distribution with RMS equal to a amplitude of signal from 2000 electron in the tube -

---

<sup>2</sup>in this equation  $t$  in nanoseconds

<sup>3</sup>as in table 2

<sup>136</sup> electric noise charge (ENC)<sup>4</sup> On Fig.5 you can see deposition from noise marked by blue line.  
<sup>137</sup> On the Fig.5 the timestamp *Time* = 0 corresponds to the time when muon hits a tube.  
<sup>138</sup> The convolution function smooths and spreads input current. It mean that the output voltage  
<sup>139</sup> in GARFIELD does not contain part of signal before hit event timestamp.

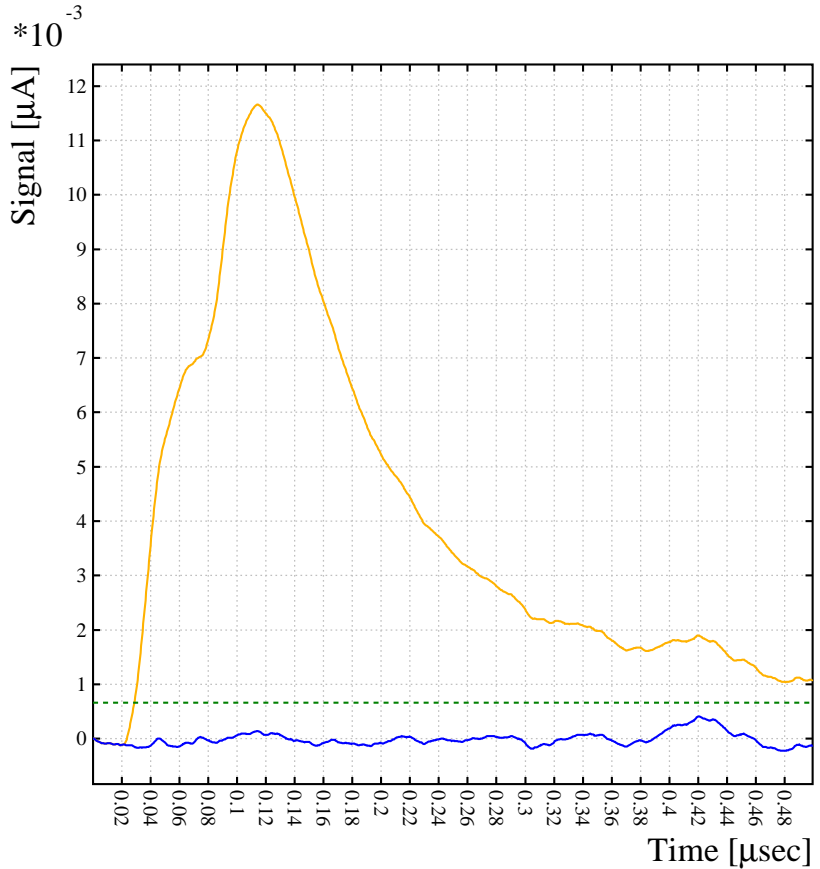


Figure 5: Example of output signal  $V(t)$  after convolution (front-end electronics) from central track (yellow line). The noise component of the same signal depicted by separate blue line. Grin dashed line is a threshold for trigering drift time and equals to  $5\sigma$  of noise distribution.

### <sup>140</sup> 3.2 STRAW efficiency

<sup>141</sup> The interaction of charge particle with gas molecules has probabilistic nature. For short dis-  
<sup>142</sup> tance tracks (somewhere near the tube wall) the probability of tracks that generation of zero  
<sup>143</sup> electron/ion pairs becomes significantly high.

<sup>144</sup> The number of produced ionization clusters directly affects the hit efficiency profile. Smaller  
<sup>145</sup> ionization length increases the hitting efficiency because of production more ionization clusters  
<sup>146</sup> per length unit [4]. In GARFIELD we can easily calculate amount of clusters per track. In

---

<sup>4</sup>With testing of real 5 m long straws and ultimate examples of electronics we will measure real noise. But for now it is only close to reality suggestion concerning to this issue.

<sup>147</sup> Fig.7b you can see a distribution of number of clusters per central track for our STRAW tube.  
<sup>148</sup> It means that straw efficiency will be lower near the tube wall (see Fig.6).

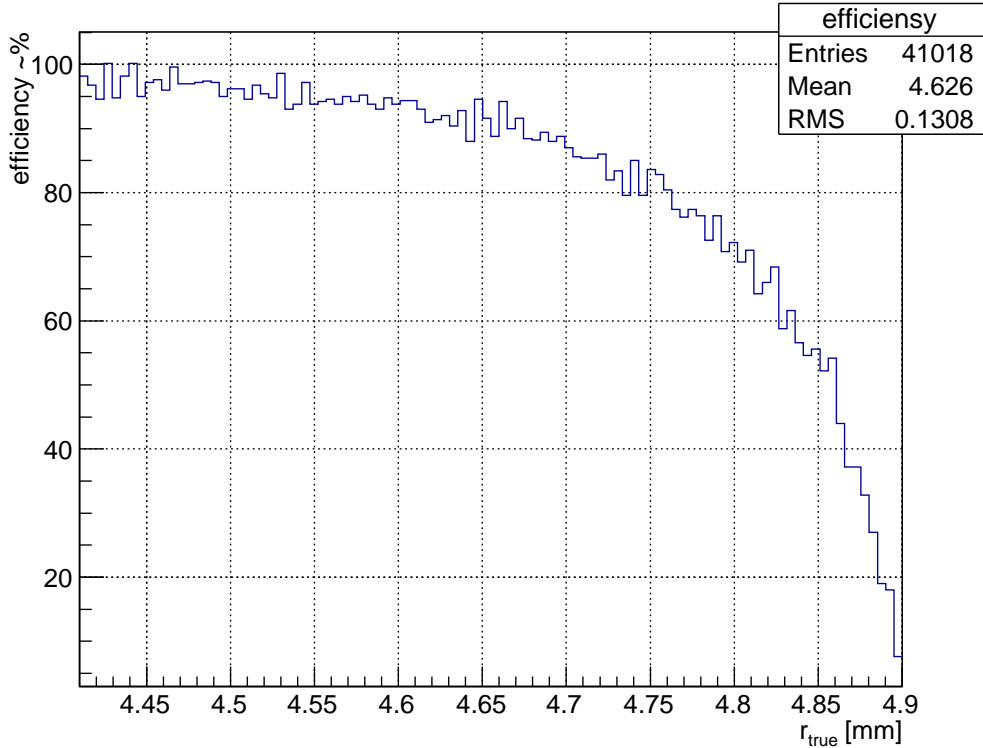


Figure 6: Straw tube efficiency. Result of homogeneous penetrating periphery of tube by 50k events (scaled down by factor of 5.  $\frac{50k \text{ events}}{100\text{bin}} = 500 \frac{\text{events}}{\text{bin}}$ ).

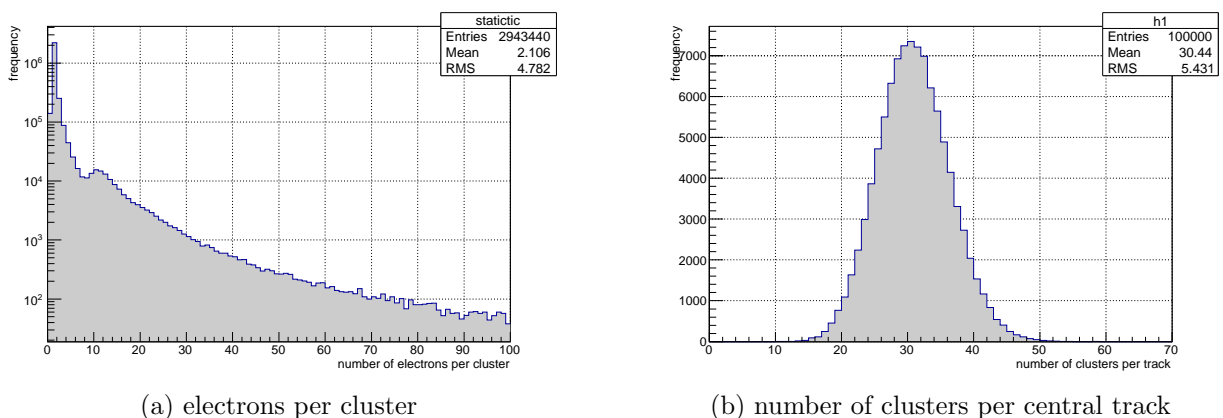


Figure 7: Statistics info from GARFIELD about track from  $1GeV \mu$ . Tube described in table 2

<sup>149</sup> From the Fig.6 we can conclude that the efficiency of tube is 100% almost in whole region

150 covered by tube except pre wall region which is quite small. Increasing the gas mixture density  
151 or increasing the tube radius for the same gas density can increase tube efficiency.

## 152 4 Gain

153 Lets look on avalanche process in the tube. If multiplication occurs, the increasing of the  
154 number of electrons per path  $ds$  is given by

$$dN = N\alpha ds \quad (2)$$

155 The coefficient  $\alpha$  is determined by the excitation and ionization cross sections of the elec-  
156 trons that have acquired sufficient energy in the field. It also depends on the various transfer  
157 mechanisms and electric field  $E$  and increases with the field because the ionization cross-section  
158 goes up from threshold as the collision energy  $\varepsilon$  increases. As we can suppose the coefficient  $\alpha$   
159 is of big amount of parameters.

160 The amplification factor  $G$  on a wire(that is more interesting for us) is given by integrating  
161 (2) between the point  $s_{min}$  where the field is just sufficient to start the avalanche and the wire  
162 radius  $a$ :

$$G = N/N_0 = \exp \int_{s_{min}}^a \alpha(s) ds \quad (3)$$

163 GARFIELD can provide us by amplification factor  $G$  for any point of the tube(because  $G$   
164 is coordinate dependent magnitude). The amplification factor is equal almost in whole tube  
165 space except neighbourhood near the wire because electric field becomes significantly high only  
166 near the wire (see figs 8a, 8b). When the wire is shifted from the center of the tube the electric  
167 field in area close to the wire is the same as in centered state. So the amplification factor  $G$  is  
168 quite similar in both cases.

169 Implementation of gain value calculation is not so reliable in GARFIELD(especially for-  
170 tran version). Gain should be recalculated using Garfield++ (which is newer and takes into  
171 consideration more effects).

172 On the Fig.9 you can see that the gain  $G(V)$  have precisely exponential dependence. This  
173 is frankly does not inspire confidence. The difference can be up to 100% (as Rob Veenhof -  
174 creator of GARFIELD [3] said).

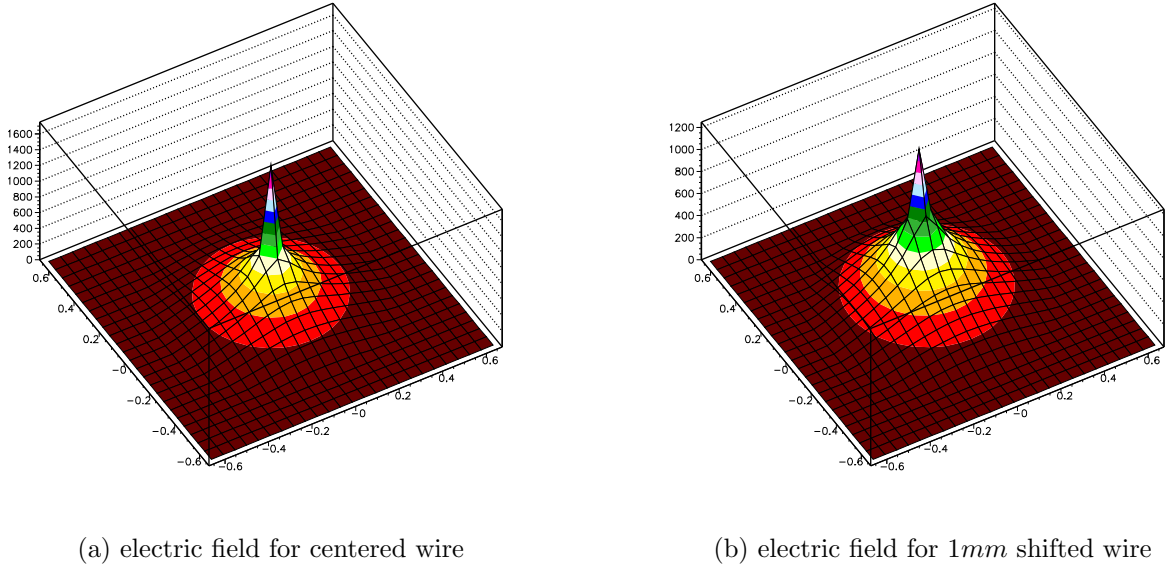


Figure 8: Electric field intensity map for different wire position in the cube calculated in GARFIELD software. Conditions for those plots are described in table 2

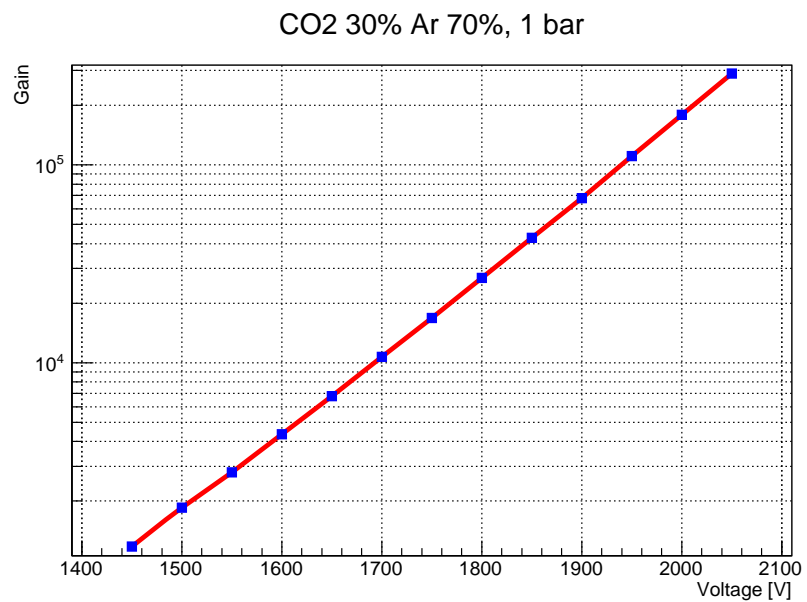


Figure 9: Dependence of the gain of the voltage applied to the wire. The rest of STRAW tube settings corresponds to table 2.

## 175 5 Wire sagging

176 Easy to predict that the displacement of the wire invokes distortion an electric field (see  
 177 figs 8a,8b) and drift path for electrons/ions inside the tube (see fig.10a and Fig.10b). The  
 178 RT-relation for track reconstruction directly depends on the wire position in the tube. So  
 179 RT-relation loses it's previous symmetry (see next sections).

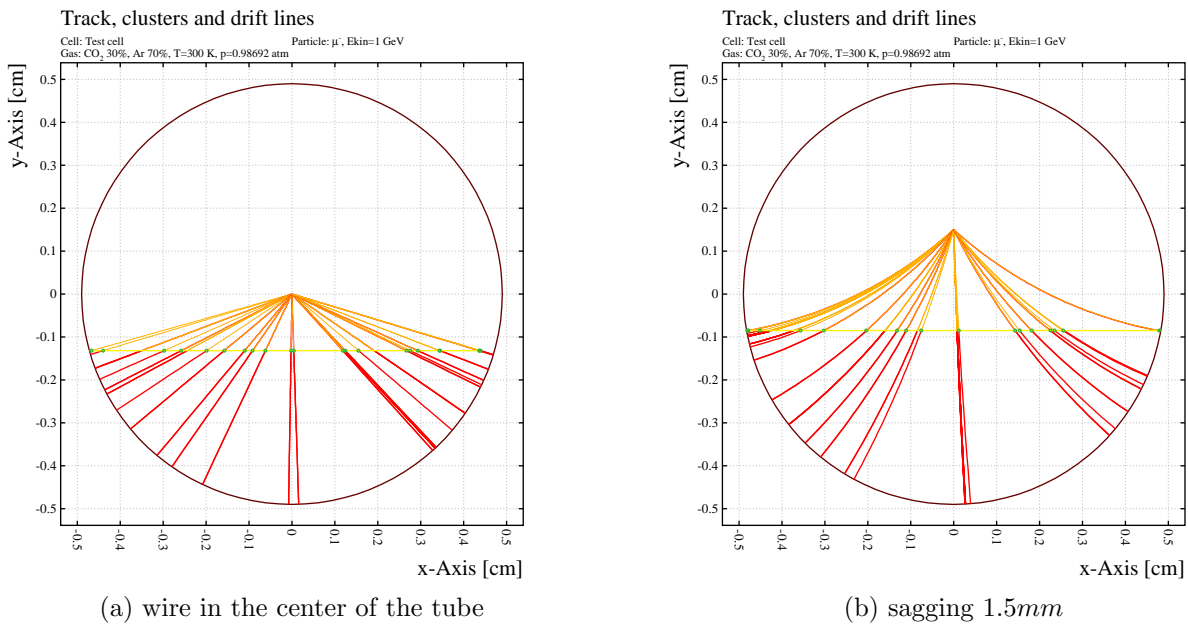


Figure 10: An example of tracks from the on the tube for different position of the wire from GARFIELD simulations. Initial clusters marker by green. Drift lines for electrons marked by yellow, ions – red lines.

180 The direction of sagging is unpredictable when the wire is centered and the straw has vertical  
 181 orientation. Impact of gravitation field into the wire does not make any effect in this state.  
 182 But we can avoid this ambiguity by setting straws horizontally. This condition is necessary  
 183 to make track reconstruction possible. Even when strung with a pulling force  $T$  close to the  
 184 breaking limit, wires in several metre long tubes will experience a gravitational sag that is large  
 185 in comparison with the achievable accuracy of drift tubes.

186 We estimate significant wire sagging(by comparison to the tube radius) because of wire  
 187 attraction to the tube under affecting of gravitation and electric field force.

188 You can see a profile of wire sagging of 5m length wire in 1cm diameter straw tube and  
 189 1750V voltage on the Fig.11 calculated in GARFIELD software [3].

190 The calibration of STRAW tube with sagged wire is more difficult by comparison to the  
 191 mode without sagging.

192 Variation of wire tension, wire radius should be taken into account as high affect factor for  
 193 sag value.

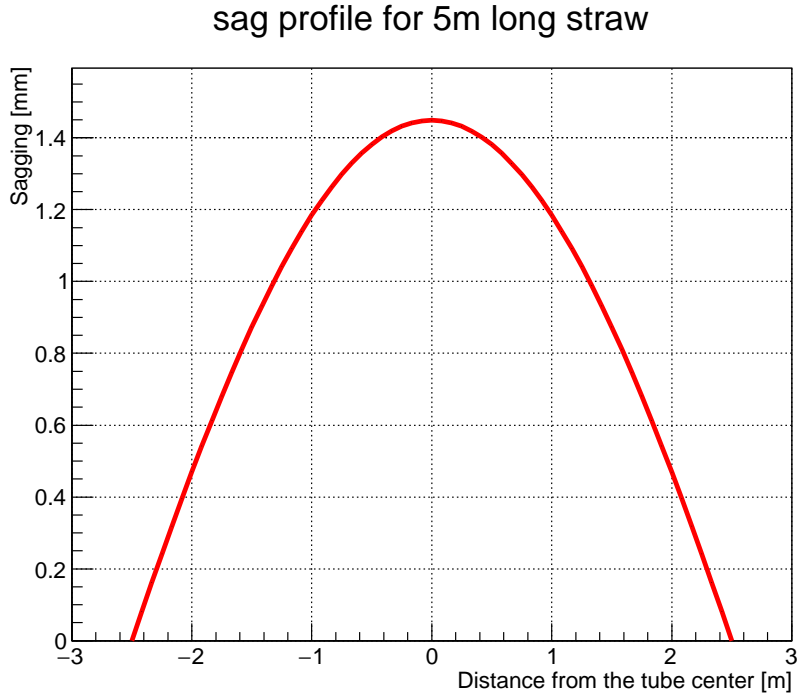


Figure 11: Wire sag profile under electric and gravitation field calculated in GARFIELD. All options for this straw system are described in table 2.

## 194 6 Sag estimation

195 In this section we have to find out method for assessing sagging. This is key step that makes  
 196 track reconstruction procedure possible.

197 At first we have to think on data we can use for such kind of calculations. We can extract  
 198 much useful information from drift time distribution.

199 The wire sags under electric and gravitation force. Therefore the sag value differs along  
 200 the tube (Fig.11). But we can separate collected data for different position along the tube.  
 201 STRAW tube detector consists of several parallel layers of tubes at some angle to each other.  
 202 So we can easily fix longitudinal position (along the tube) for tracks that cross several crossed  
 203 tubes (at least two). Collimation is also possible via scintillator triggering before and after  
 204 STRAW tube.

205 Lets say we can install our STRAW tube into homogeneous particle flow and save drift time  
 206 distribution for some narrow section of the tube. These distributions are different from each  
 207 other(see example on Fig.12). The difference between diagrams increasing with sag difference.  
 208 So it is good tools for sag calibration.

209 Then we have to bind each drift time distribution with appropriate sag value. This is part  
 210 of laboratory work when sag profile measurements can be performed via optical method prior  
 211 to the exposition.

212 GARFIELD can handle only two-dimensional tasks. So every simulation in this article is  
 213 plane - as shown in Fig.10a. Distributions on Fig.12 contains GARFIELD simulations for tube  
 214 with wire located at certain position (in terms of displacement from tube center).

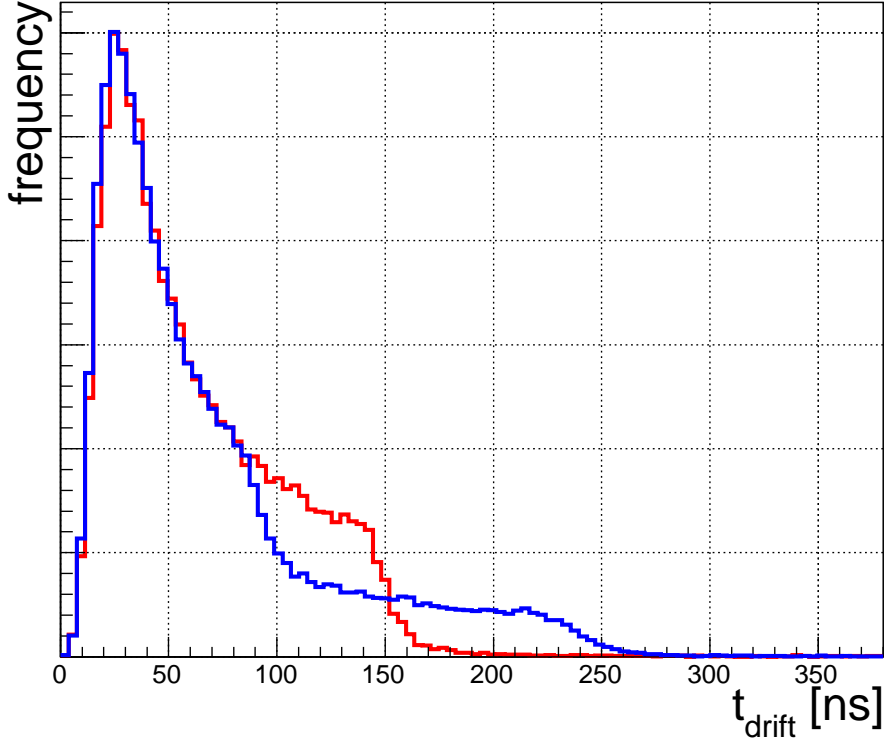


Figure 12: Drift time distribution for a homogeneous irradiation with a centered wire (red) and for a wire offset of 0.9 mm (blue).

Lets say we have an equipment for scanning the tube to measure wire sagging profile. After profile measurements we divide our tube into sections. Wire position within separate section should be defined within desired precision

So we need divide our tube on 57 sections (see Fig.13) if maximum of wire offset (at the center of the tube) is equal to 1.45mm and desired precision is 50 $\mu$ m.

$$N_{halftube} = \frac{1.45\text{mm}}{50\mu\text{m}} = 29; \quad (4)$$

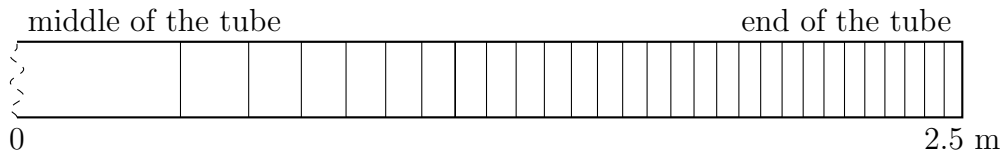


Figure 13: Tube sectioning. Sag value at the tube center is 1.45mm. Difference of wire sag value from section to section is 50 $\mu$ m

Then we need an exposition of sufficient number of events for every of sections (at least 50k events). There can be troubles time of exposition time because square of sections at the end

222 of the tube is quite small. So the time of exposition of distant sections will be inversely much  
223 longer.

224 The next step is to find dependence of DT-distribution shape with wire offset. The point  
225 that we can evaluate matching between histograms via  $\chi^2$  criteria. As we can see in the Fig. 14a  
226 the comparison of  $\chi^2$  has smooth dependence across increasing of wire offset for high statistic  
227 histograms.

228 First steps for sag estimation are:

- 229 1. measure wire sag profile via optical method;
- 230 2. make a sectioning of tube due to wire sag profile;
- 231 3. collect enough amount of events for every of dt-distribution and save this *core* distribution  
232 for further comparisons.
- 233 4. measure DT-distribution of tube section that is subject of study and adjacent area.
- 234 5. calculate  $\chi^2$  criteria for this current dt-distribution with each of core distribution.
- 235 6. correlate found values of wire displacement relatively to the adjacent sections or by fitting  
236 of whole wire profile points.

## 237 **6.1 Finding most probable value of wire displacement for certain 238 point of the tube**

### 239 **6.2 Raw method**

240 The simplest method to find  $S$  is to equate it to the corresponding value of best matched core  
241 DT-histogram.

242 On the figure 14b you can see distribution of such kind of reconstruction. The precision can  
243 be quite high ( $\sim 50\mu m$ ) even for DT-distribution with 5k events. This method is limited by  
244 core DT-diagram stepping.

### 245 **”Minimum of $\chi^2$ as linear approximation”**

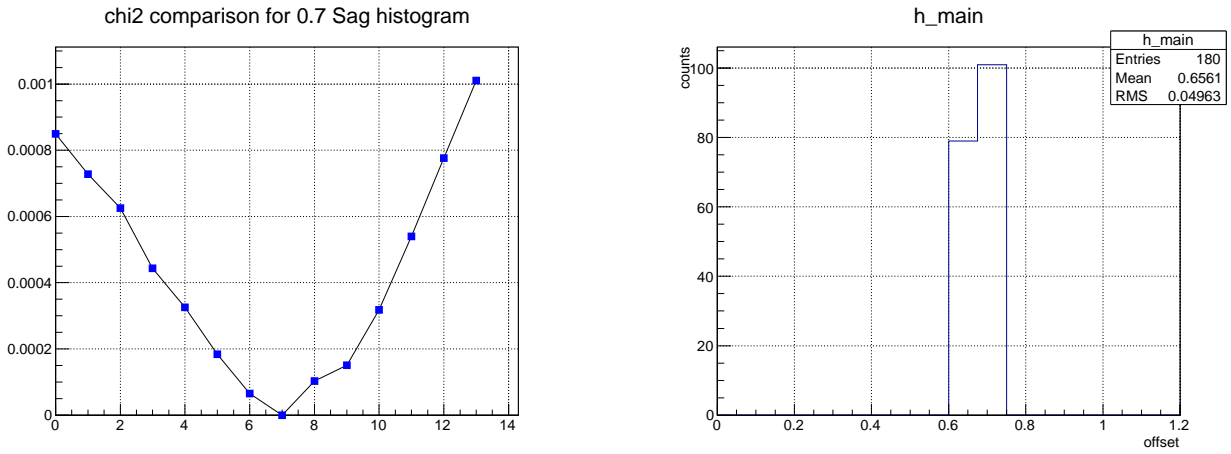
246 If dependence of  $\chi^2$  criteria of wire displacement  $S$  for near to the true position region is  
247 linear (that certainly is not a true, but as first approximation) than we can easily find this  
248 intermediate value of wire displacement.

249 There we proceed in two steps. The first is raw estimation of wire displacement as in above  
250 mentioned method.

251 For the second step we need to know some additional estimations. The first question is how  
252 small can be  $\chi^2$  in our case? Lets fix statistic on 50k events for one DT-distribution. This  
253 value should a bit depend for different  $S$ . But for now lets consider that it is a constant value.  
254 From the Fig.15a you can see distribution of  $\chi^2$  from comparison of 20 DT-distribution<sup>5</sup> for  
255  $S = 0.7mm$ . Mean value + RMS of distribution is  $5.3 * 10^{-5}$ . So if some of the  $\chi^2$  is higher  
256 than this threshold than we go for second stage.

---

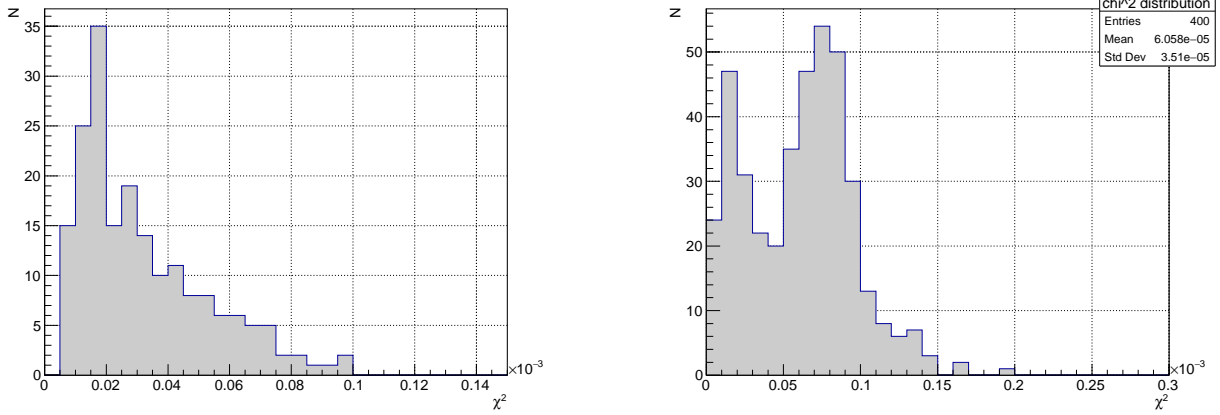
<sup>5</sup>pair comparison give us  $C_{20}^2 = \frac{20!}{2!18!} = 190$  different combinations



(a) Series of  $\chi^2$  of comparison 0.7mm sag core td-distribution with each of core histograms. 14 core histograms for sag range 0 ... 1.3mm with stepping of 100 $\mu\text{m}$

(b) Distribution of wire offset reconstruction from 180 series 5k events each. 50k events for core template histograms. True bias is 0.63mm. 1 bin = 0.1 mm.

Figure 14: Wire position(displacement) reconstruction



(a)  $\chi^2$  distribution of comparison of 20 DT-distributions diagrams each other ( $C_{20}^2 = 190$  combinations)

(b)  $\chi^2$  distribution of comparison DT-distribution histograms 0.6mm S vs 0.7mm

Figure 15: Comparison of  $\chi^2$  distributions for self-comparison of DT-distribution diagram.

In the Fig.14b you can see distribution of wire sag calculation for 180 histograms with 5k events statistic. Precision in this case  $\sim 50\mu\text{m}$ . The algorithm of sag estimation is pretty simple: wire offset value is equal to the offset of best matched core histogram.

After that we know sag value at series points of the tube. Then we can find whole sag profile as fit of these points by curve with several free parameters.

From the Fig.15b the distribution of  $\chi^2$  for adjacent point have narrower distribution by comparison to "self-comparison"  $\chi^2$  distribution. Therefore calculation of  $S$  from analyse of consecutive smallest  $\chi^2$  values can improve precision.

265    **6.4 Practical measurements of DT-distribution**

266    We need second detector that can measure position of muon that hit STRAW tube. It can be  
 267    Si strip sensor based detector or detector based on scintillation with the same destination.

268    Each kind of detector have it's own advantages and disadvantages. The potential cell unit  
 269    (strip of pixel) of Si detector will be smaller than in scintillator but also is much expensive. At  
 270    the current stage we deal with 1cm diameter tubes. So scintillator is primal target. But it can  
 271    shift to the Si sensors if scintillators will not provide satisfied precision.

272    Preliminary scheme of DT-measurements you can see on the picture Fig.16

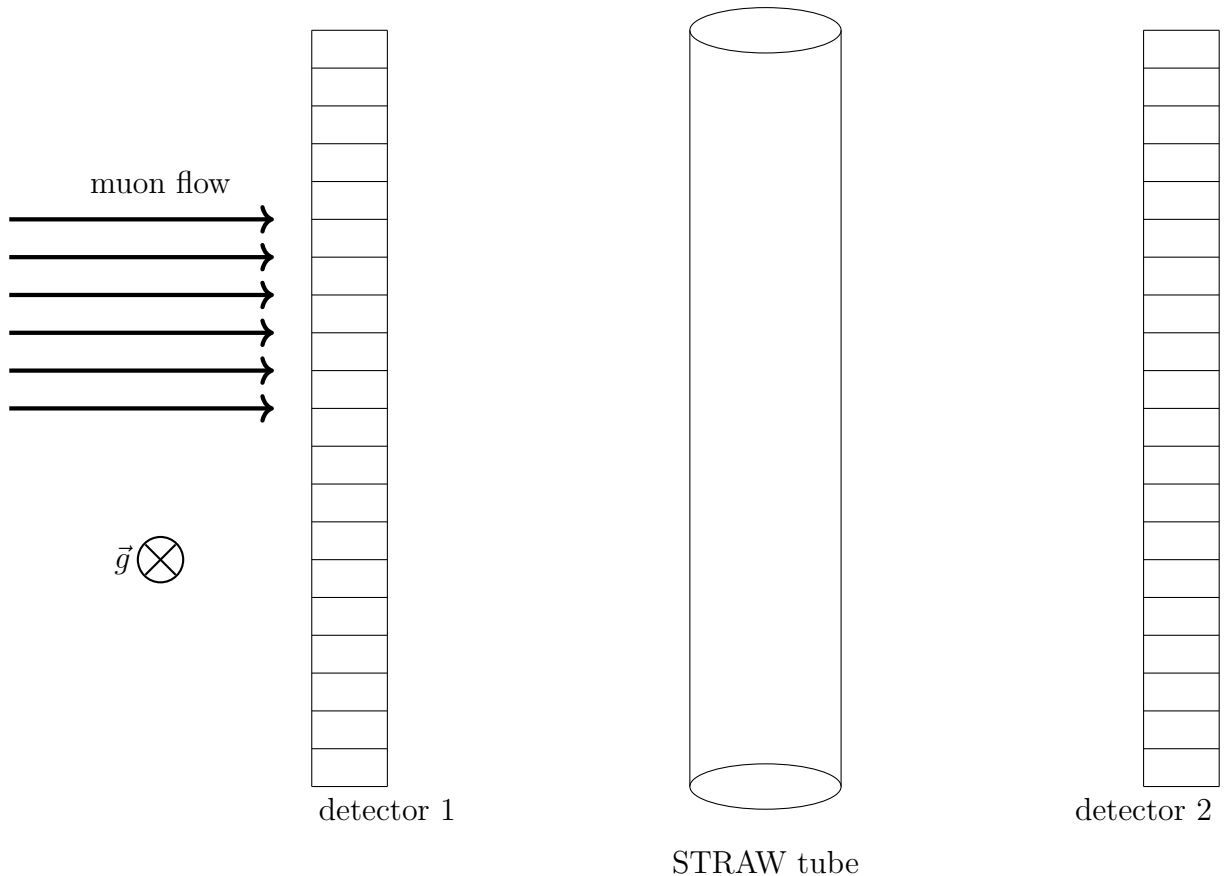


Figure 16: principal layout of measurement of core DT-distribution histogram

273    In this method detector before tube (D1) and detector placed after the tube(D2) in total  
 274    should provide sufficient precision for track reconstruction to be able distinguish tracks for  
 275    different section of the tube (approximately as shown on the Fig. 13). Muon flow should be  
 276    homogeneous and so D1 and D2 also should cover full acceptance of the tube.

277    The profile of the wire sagging can be measured by optical method. Walls of the tube is  
 278    very thin, so it can be simplest way to get sag profile.

## 279 7 Track reconstruction

280 The time between the track hit time stamp and the signal rising edge is a measure of *drift time*  
 281 of these electrons. The relation between the *drift time* and the distance from the track to the  
 282 center of the tube(wire while no sag for centered wire) is called *drift time - distance* relation or  
 283 *tr-relation*.

284 The drift time  $t$  is a function of track position (relative to the wire) and electric field along  
 285 the drift trajectory.

286 One assumes that the working position for straws will be perpendicular to the particle flow,  
 287 and acceptance of particle spreading will not be significantly big. So tracks will be collinear  
 288 each other within every separate STRAW tube unit.

289 Summing the above mentioned we have one dimension task – reconstruct tracks on vertical  
 290 axis<sup>6</sup> (see examples of outcome tr-distribution  $t = t(r, s = 0)$  in Fig.17a and Fig.17b) even the  
 291 wire sagging. Sagging will be always down thanks to gravitation force  $\vec{g}$ .

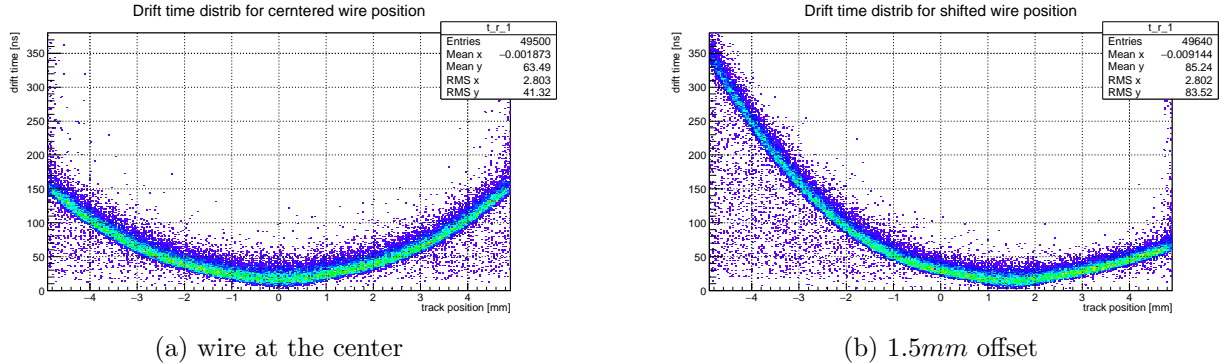


Figure 17: Distribution of drift time  $t_{drift}$  as function of track position  $r_{track}$  relatively to the tube center

292 The rt-relation varies along the tube according to wire displacement  $s$ . Thus we have for  
 293 the drift time:

$$t_{drift} = t_{drift}(r_{track}, s) \quad (5)$$

294 The idea is to find the inverse dependence

$$r_{track} = r_{track}(t_{drift}, s) \quad (6)$$

295 From Sec.6 we can find sag profile for straw. Therefore the rt-calibration becomes 1 dimension-  
 296 less for every certain value of wire displacement  $s_0$ :

$$r = r(t, s = s_0) \quad (7)$$

---

<sup>6</sup>An example of single track reconstruction which explains the approximate procedure of reconstruction you can see on Fig.4

## 297 7.1 How drift time resolution depends on wire offset?

298 Deformation of electric field inside the tube invoked by wire displacement from the center  
 299 position affects drift time. Here we are going to estimate magnitude of drift time change.

300 As was noted above we make a binning for our data along the  $r_{track}$  (Fig.17a,17b). Resolution  
 301 equals to RMS at every bin of digram (Fig.18).

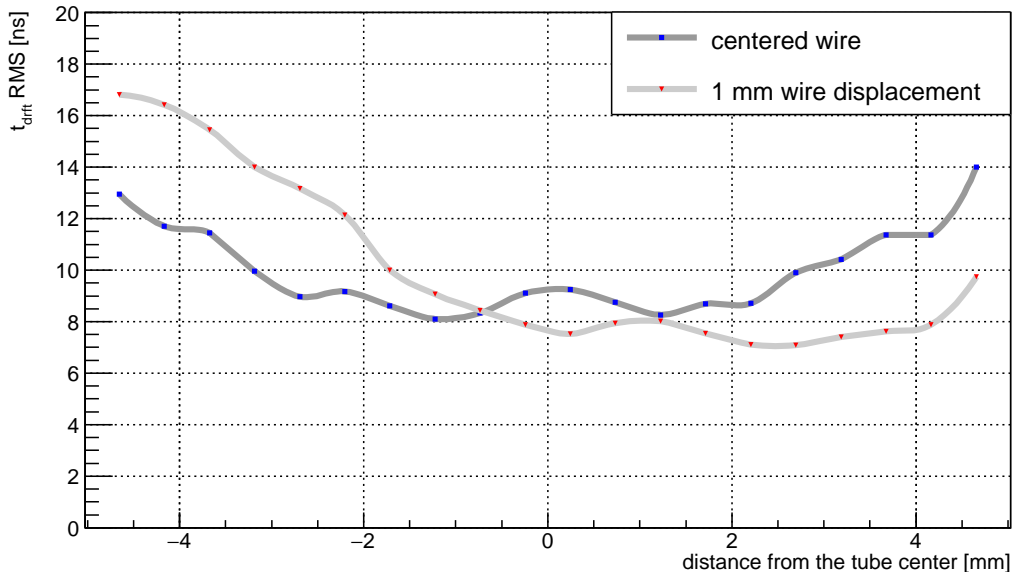


Figure 18: Resolution of drift time as a function of distance from the wire.

302 We are dealing with probabilistic nature of clustering that spread RT-relation from thin  
 303 line. The leakage noise is also present in calculation but the effect is not very high (especially  
 304 in this calculation).

305 Every plot of output current (see fig. 5) consist of 1000 equidistant frames. The threshold is  
 306 set to  $5\sigma$  of noise. Leakage noise make effect on drift time measurements in case its amplitude  
 307 becomes higher than threshold value in range from  $t = 0$  to  $t = t_{drift}$ . At five-sigma there is  
 308 only one chance in nearly two million that a random fluctuation would yield the result. The  
 309 drift time for tracks close to the tube edge can be up to 150ns and 300ns in case wire displaced.  
 310 The probability to meet noise above threshold value is less than 0.02%.

311 Another source of noise points on TR-distribution comes from  $\delta$ -electrons that cause sec-  
 312 ondary ionisation in tube volume. Only those electrons make impact which are emitted in the  
 313 direction of the wire(see example on fig.19a).

314 The number of events out of TR-ralation caused by  $\delta$ -electrons is quite small. Especially  
 315 percentage of events where  $\delta$ -electrons make effect on drift time is less than 1% of total number  
 316 of events in GARFIELD simulations.

317 Tube wall is very thin but particle still can cause  $\delta$ -electrons when crossing it. GEANT4  
 318 studies show that such kind effect also presents in interaction of muon with tube volume, and  
 319 percentage of events with  $\delta$ -electron that affect drift time even less than 0.2%.

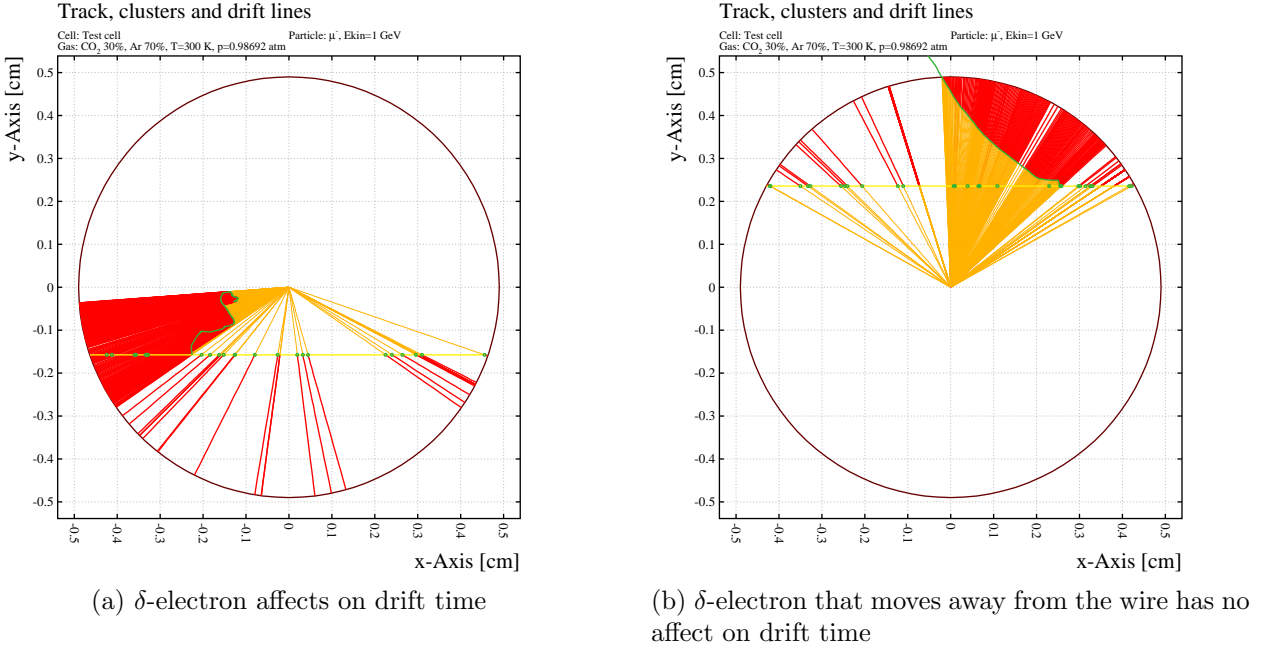


Figure 19: Garfield simulation with  $\delta$ -electron presence. Red lines - ion trajectory, yellow - electrons. Trajectory of  $\delta$ -electron marked by green curve line.

## 320 7.2 Finding of rt-relation

321 The RT-relation depicts relation between drift time and track position. The idea is to find the  
322 best fit of give data to achieve higher resolution and avoid systematic errors.

323 The problem is in that we have to minimize influence of noise while fit. One suppose that  
324 the noise has approximately homogeneous distribution of points that locates below the main  
325 line of distribution. Consequently we can filter it by fitting only points from regions with local  
326 point density higher than some threshold value. Another way is to make a binning of our  
327 distribution along the track position and fit every 1D histogram by Gaussian. The fit points of  
328 Gaussian mean values by fit function.

329 Nevertheless our data contain very small amount of "non-track" points.

330 TR-relation is asymmetry relatively to the  $r = 0$  almost in all cases except wire in the center  
331 of the tube. Therefore we have to calibrate for every of branches. It means we need to find two  
332 track positions for every of drift time value and reject one of them in further data processing  
333 stages.

334 In previous section we found way to measure wire sag profile. So we can use this trick in  
335 present stage for separating data into "right" and "left" branch. Every of branches we will  
336 calibrate separately.

337 Lets suppose we can fit every of TR-diagram by pair of analytic fit functions (8):

$$t(r_{track}) = e^{a_0 + a_1 r_{track}} \quad (8)$$

338 If the Fig.20 you can see TR-relation. Fitting is not perfect because of using simple fit  
339 function template (8). But we will use reverse to the (8) relation, because we have to find  $r_{track}$

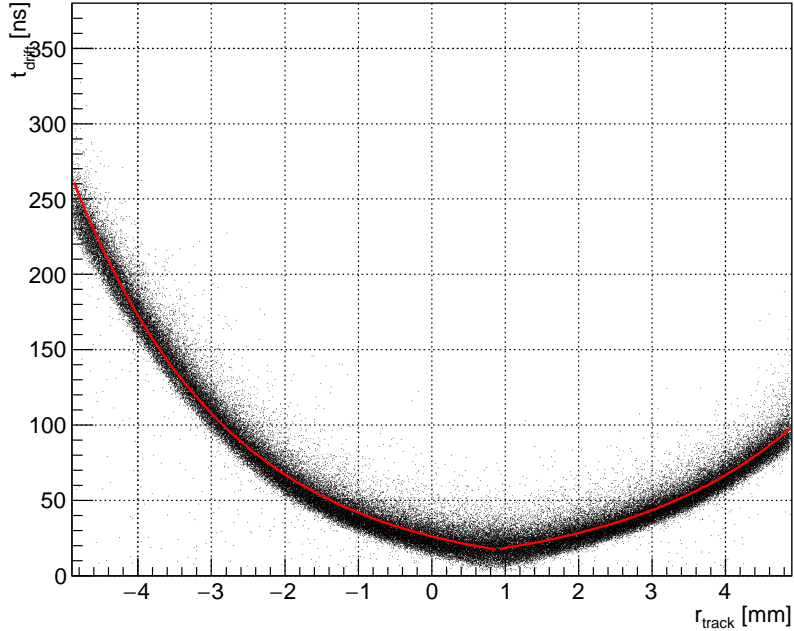


Figure 20: TR-relation fitting for 0.9mm wire offset value

340 from known  $t_{drift}$ . We can do it because the aim of this studies is not a precise calibration  
 341 but global evaluation effect of wire sagging into total result.

342 As you can see in the Fig.20 red fit line does not cover whole drift time spectre. So events  
 343 with drift time less than covered range(less than  $\sim 20\text{ns}$ ) counts as track through the wire:

$$r_{track}(t_{drift} < t_{min}) = r_{wire \ pos} \quad (9)$$

344 where  $t_{min} = \min(t_{drift}(r_{track}))$ ,  $r_{track} = \overline{(-r_{tube}, r_{tube})}$ . Respectively tracks with drift time  
 345 higher than maximum of fit function range is artificially counted as tracks with near tangents  
 346 to the tube position  $r_{track} = \pm r_{tube}$  (because efficiency decreases near the tube wall down to  
 347 20%).

### 348 7.3 Track reconstruction precision

349 Obviously the precision is the main factor in design of detector.

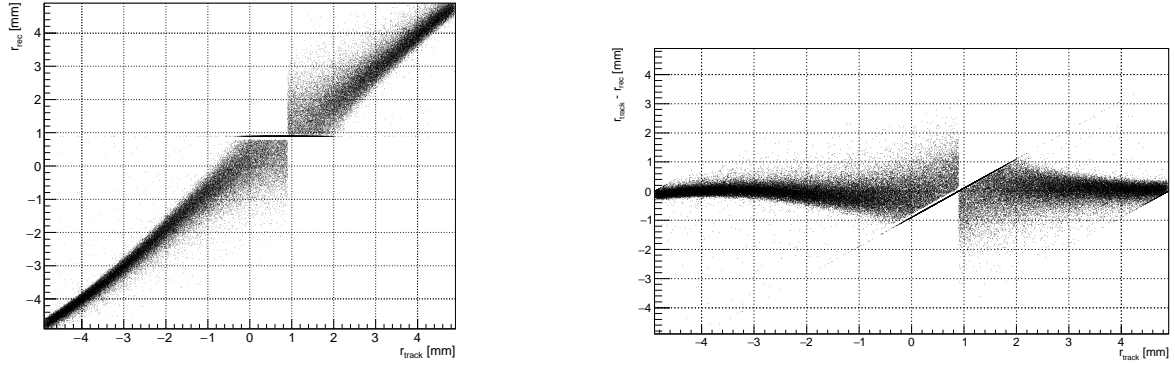
350 The STRAW tube tracker should be as light as possible to avoid multiple scattering on  
 351 structural components of detector. But design should be changed within reason if precision  
 352 suffers from this<sup>7</sup>.

353 How precision of track reconstruction depends on wire position(wire displacement)?

354 As you can see on Fig.22 there are no significant difference of track reconstruction preci-  
 355 sion between two mode of wire location despite of the increasing drift time for displaced wire  
 356 position(with almost factor of two). The highest resolution( $\sim 0.1\text{mm}$ ) near the tube wall and

---

<sup>7</sup>Especially design with no sagging works well for experiment NA62 [1]. But they have more than 2 times shorter straw when tube have insert in the middle of the tube. So sagging becomes negligible in this case.



(a) reconstructed track position  $r_{rec}$  as function of true track position  $r_{track}$

(b)  $r_{track} - r_{reconstructed}$  as function of  $r_{track}$

Figure 21: Distributions of matching of track position to their reconstructed value.

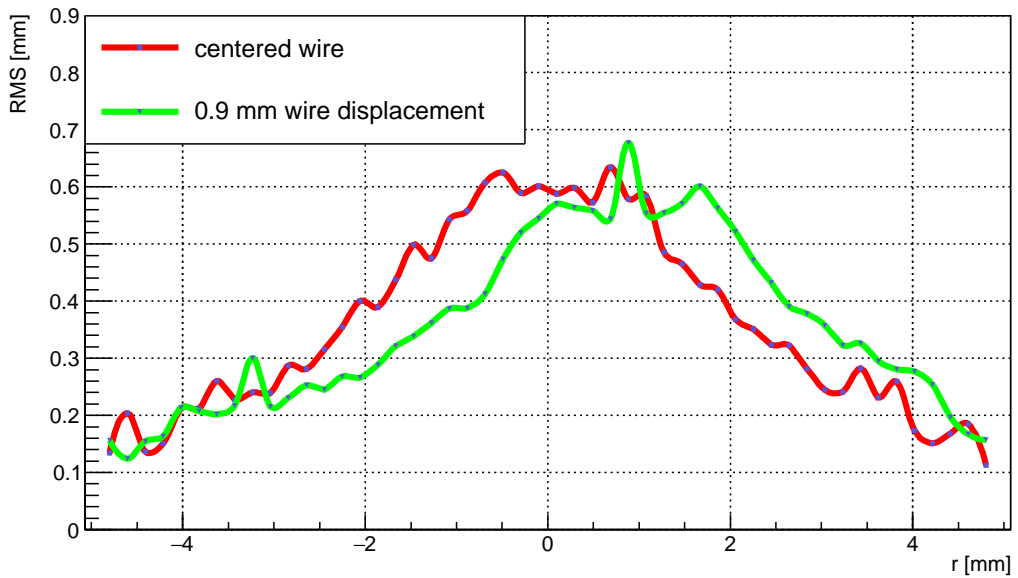


Figure 22: Comparison of track reconstruction precision for two wire position. Value of precision at every point means RMS of data sample near corresponding track position  $r$ . Red line corresponds to the centered wire position, green line – to the 0.9mm sagged wire position.

357 worst value  $\sim 0.6mm$  is near the wire because the clustering effect. Higher gas pressure should  
 358 resolve this problem.

## 359 8 Measurements

360 We made measurements of some important drift tube parameters. We had tube of  $\sim 50\text{cm}$   
 361 length. But despite of short tube length we made measurements where the length of the tube  
 362 is not important.

363 The tube was manufactured in Dubna(Russian Federation) and was placed into the appro-  
 364 priate mechanics which include tube fixing, channels for supply of gas mixture, connector for  
 365 grounding to the tube walls and connector for High Voltage (HV) supply.

366 The whole system is not compact, therefore we could not avoid the parasitic capacities. Now  
 367 we will not go into details about it, as we have nothing to compare with because the system is  
 368 non-separable.

369 The scheme of gas supply, circulation and control in the tube is shown in the Fig.23.

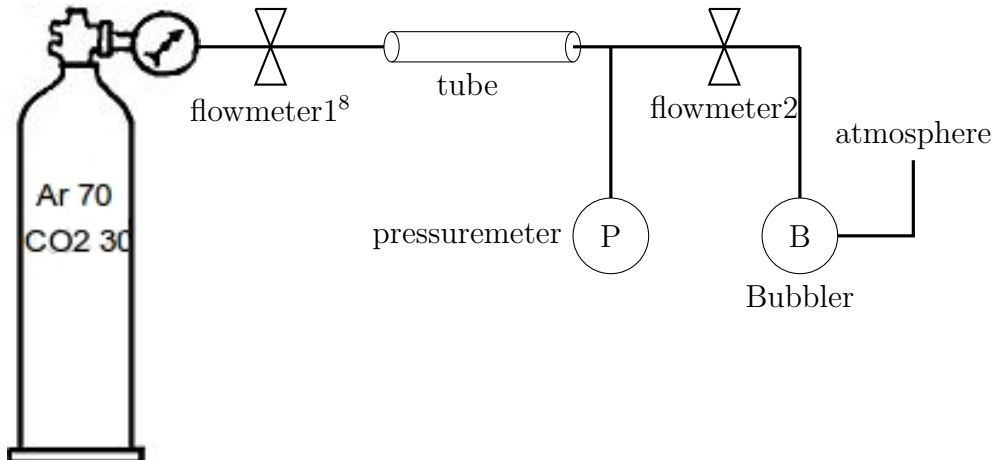


Figure 23: Gas circulation scheme and circuit of connection of flow control through the drift tube

370 The electric scheme of the drift tube connection is shown in the Fig.24.

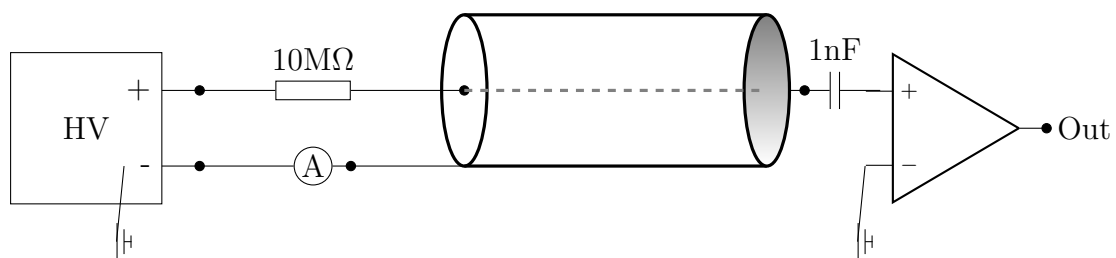


Figure 24: The electric scheme of the drift tube connection

371 As it is seen above, the scheme is very simple.

372 For our research we used a source  $Fe^{55}$  which is suitable for a drift tube calibration. In our  
 373 case  $Fe^{55}$  serves as a photon source with almost monochromatic spectra with energy 5.9 keV.

374 The most important parameter which we have to measure is Gain  $G$  (3).

375 The idea is to measure a charge that goes through the tube electric circuit per unit of time  
 376 and then find Gain. We assume that a current  $I_0$  through the ampere meter(see fig. 24) is

377 constant when the radioactive source is absent. The current is non-zero when the tube detects  
 378 background particles(for example atmospheric muon flux) or when a leakage current is present.  
 379 Therefore, with the presence of a source  $Fe^{55}$  all surplus of the current  $\Delta I = I - I_0$  in the drift  
 380 tube circuit occurs because of gamma ray detection.

381 On the other hand, we can write  $\Delta I$  in terms of initial amount of electrons and Gain in the  
 382 following form :

$$\Delta I = GN_0e, \quad (10)$$

383 where  $G$  – Gain;  $N_0$  - number of initial electron-ion pairs per second;  $e$  - charge of electron  
 384 in C.

385 On the other hand we can express  $N_0$  as:

$$N_0 = R \cdot \langle n \rangle = R \cdot \sum_n np(n) \approx R \int_0^{\infty} np(n)dn; \quad (11)$$

386 where  $p(n)$  is a probability that the photon with energy 5.9 keV after interaction with  
 387 argon atom will create  $n$  electron-ion pairs;  $R$  is a rate [Hz], as we need to find the amount of  
 388 electron-ion pairs per one second.

389 The calculation of the distribution  $p(n)$  in GARFIELD is shown in Fig.???. In the figure  
 390 we can see the two peaks: the main photopeak and the smaller escape peak. The escape peak  
 391 for argon is known to be 3.2 keV less than the primary peak. An escape peak is formed by  
 392 a number of photon interactions in the gas resulting in one primary ionization electron and a  
 393 re-emitted X-ray with a long mean free path.

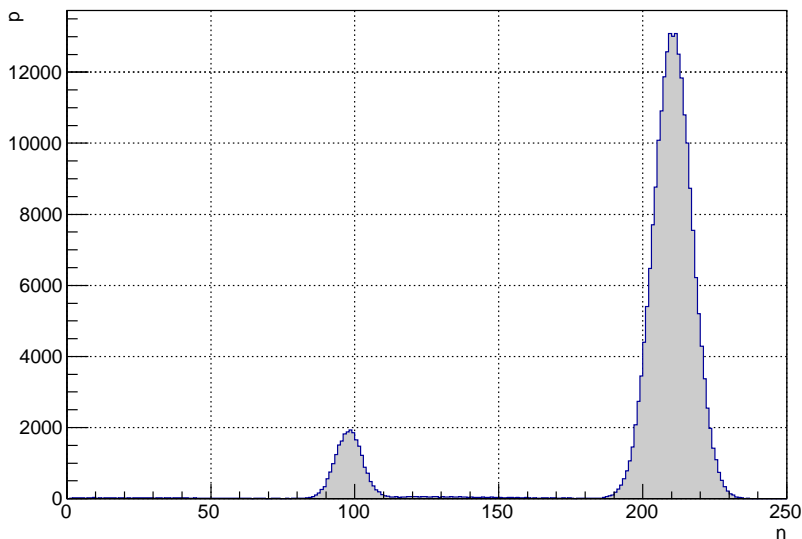


Figure 25:  $p(n)$  distribution

394 The realisation of a measurement is very simple. On the amplifier output (see Fig.24) the  
 395 signal goes to the discriminator with trigger threshold on the level enough for a signal detection  
 396 and big enough for noise neglecting. The signal from discriminator in rectangular form goes

397 into counter. The counter is triggered for the rising edge. This scheme has a small dead time  
 398  $0.5\mu s$ , therefore for the signal frequency of  $R \sim 5000 \frac{\text{events}}{\text{second}} \approx 200 \frac{\mu s}{\text{event}}$  the amount of non  
 399 counted signals is negligibly small.

400 For the first gain estimation we assume about avalanche superposition and linear amplitude  
 401 dependence of final signal on the amount of initial electrons(later we will show that this is not  
 402 true).

403 From the distribution in Fig.25 we can find  $\langle n \rangle = 197.87$  for average amount of primary  
 404 electron because of photon (5.9keV) interaction with atoms of a gas  $Ar70\% + CO_230\%$ .

405 The results of measurements are shown in the table 3. The Gain curves G(V) for several  
 406 pressure values are shown in the Fig.26.

| Gain(no cor) | P[bar] (U[V]) | HV [V] | Thr [mV] | I [nA]  | RMS [nA] | Rate [Hz] |
|--------------|---------------|--------|----------|---------|----------|-----------|
| 11138        | 1.0(0.857)    | 1600   |          | 1.7700  | 0.0919   | =         |
| 18196        | 1.0(0.857)    | 1650   |          | 2.8915  | 0.1598   | =         |
| 29255        | 1.0(0.857)    | 1700   | 32       | 4.6490  | 0.2328   | 4965.9    |
| 47012        | 1.0(0.858)    | 1750   |          | 7.4707  | 0.4380   | =         |
| 73159        | 1.0(0.857)    | 1800   |          | 11.6257 | 0.5630   | =         |
|              |               |        |          |         |          |           |
| 9885         | 1.106(0.906)  | 1650   |          | 1.6921  | 0.1099   | =         |
| 15747        | 1.106(0.905)  | 1700   |          | 2.6955  | 0.13381  | =         |
| 25275        | 1.106(0.905)  | 1750   | 32       | 4.3263  | 0.1975   | 5349.0    |
| 39887        | 1.106(0.906)  | 1800   |          | 6.8274  | 0.2841   | =         |
| 61359        | 1.106(0.906)  | 1850   |          | 10.5028 | 0.4567   | =         |
|              |               |        |          |         |          |           |
| 9260         | 1.205(0.951)  | 1700   |          | 1.6921  | 0.1053   |           |
| 14536        | 1.205(0.951)  | 1750   |          | 2.6562  | 0.1274   |           |
| 22991        | 1.205(0.951)  | 1800   | 32       | 4.2012  | 0.1900   | 5710      |
| 35777        | 1.205(0.951)  | 1850   |          | 6.5376  | 0.2880   |           |
| 54684        | 1.205(0.951)  | 1900   |          | 9.9924  | 0.5284   |           |
|              |               |        |          |         |          |           |
| 5444         | 1.309 (0.998) | 1700   |          | 1.03    | 0.06     |           |
| 8351         | 1.309 (0.998) | 1750   |          | 1.58    | 0.14     |           |
| 13267        | 1.309 (0.998) | 1800   |          | 2.51    | 0.12     |           |
| 20615        | 1.309 (0.998) | 1850   | 32       | 3.90    | 0.15     | 5987      |
| 31716        | 1.309 (0.998) | 1900   |          | 6.00    | 0.29     |           |
| 48102        | 1.309 (0.998) | 1950   |          | 9.10    | 0.38     |           |
| 69987        | 1.309 (0.998) | 2000   |          | 13.24   | 0.50     |           |
| 100751       | 1.309 (0.998) | 2050   |          | 19.06   | 0.78     |           |

Table 3: Gain measurements

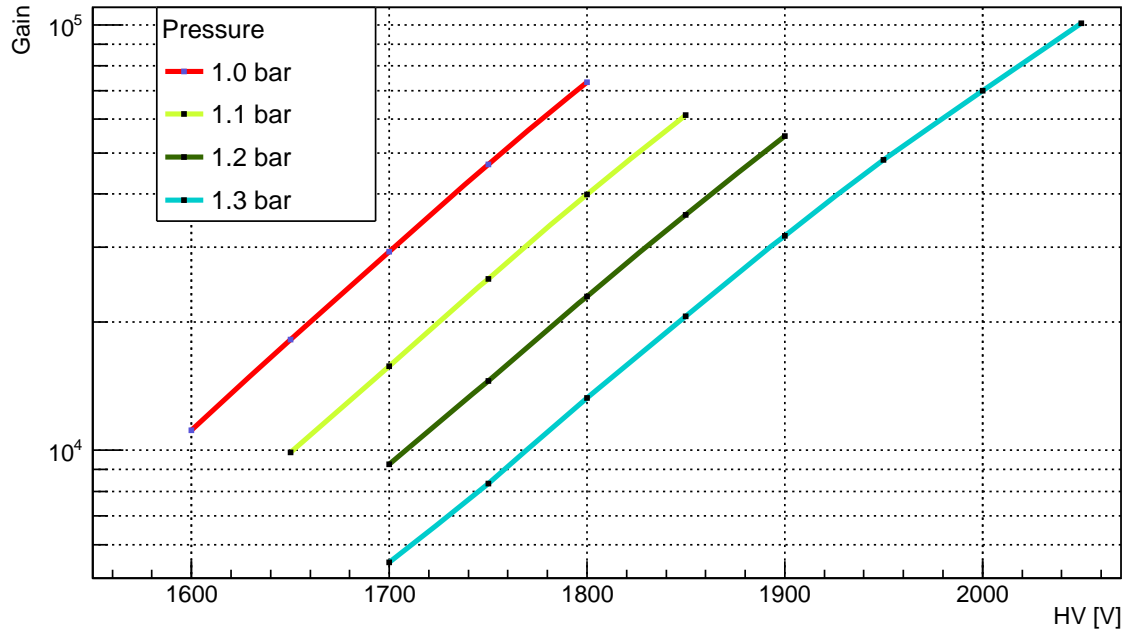


Figure 26: Gain experimental curves for several values of gas pressure in the drift tube.

## 407 8.1 Experimental spectra from the source Fe55

408  $^{55}\text{Fe}$  is a source of gamma-rays with energy of 5.9 keV. Each signal at the output of amplifier  
 409 differs by amplitude in dependence of initial electron number. Therefore, according to the cal-  
 410 culated in GARFIELD spectra  $p(n)$  (see Fig.25), it is expected to see two peaks in experimental  
 411 spectra.

412 For spectra measurements we first have to get a match between a certain signal and the  
 413 amplitude on the output of the drift tube. In our case such a quantity is an integral from a  
 414 signal on during the time of a signal.

415 The amplified signal from the output of the amplifier is sent in parallel through the linear  
 416 splitter to the discriminator and delay system. With the signal from discriminator the sampling  
 417 signal and busy signal is formed. During the busy signal the analysing system does not accept  
 418 the signal from the drift tube (this is a dead time for this detector system). The delayed  
 419 signal from the amplifier integrates during the sampling signal and then digitalizes with 10-bit  
 420 ADC. After digitalizing the signal is sent through the optical channel to PC, where the data is  
 421 recorded into separate ROOT-file.

422 The stages *sampling + storing* are time-consuming and a dead time in this case is bigger than  
 423 an average time interval between events in the tube (with current detector system) therefore is  
 424 a big probability to miss detecting an event.

425 The sampling stage is built in such a way to calibrate for pedestal shelf voltage from the  
 426 integrator. On the final histogram it will look as a small peak. We will calibrate exactly with  
 427 regard to it. The second control point is a gamma-ray 5.9 keV photo peak from the source  
 428  $^{55}\text{Fe}$ .

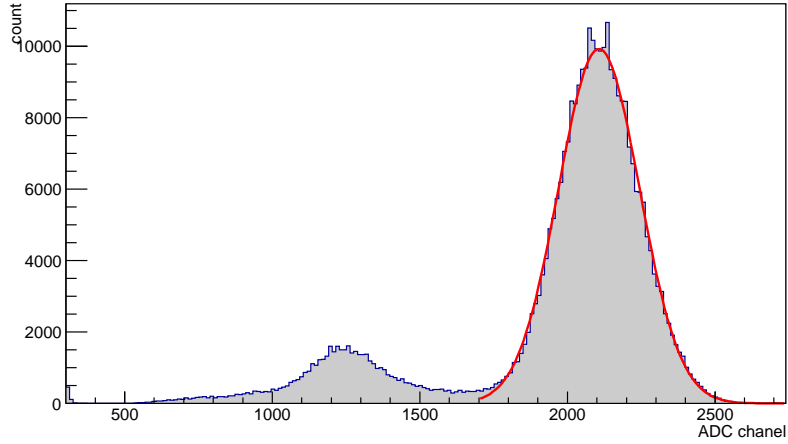


Figure 27: Experimental spectra from  $^{55}Fe$ .

| point of reference                                 | channel          | electrons per cluster(simulations) |
|--|------------------|------------------------------------|
| zero pedestal ( <i>gauss</i> $\mu \pm \Delta\mu$ ) | $301.1 \pm 0.3$  | 0                                  |
| 5.9 keV  | $2107.4 \pm 0.3$ | $210.42 \pm 0.01$                  |
| escape peak  | $1253.3 \pm 0.9$ | $97.99 \pm 0.03$                   |

Table 4: Coordinates of peaks from Fig.27 and Fig.25

## 429 8.2 Space charge effect

430 Photons from  $^{55}Fe$  of energy 5.9 keV create  $\sim 200$  electron-ion pairs as a result of photoeffect  
 431 with  $Ar70\% + CO_230\%$  gas mixture. As we have a strong electric field between anode and  
 432 cathode such electron cloud starts to drift toward a wire. The external field distorts as any  
 433 space charge creates its own e/m field. As a result, partial avalanches per initial electron of  
 434 a cloud creates an avalanche of size smaller than from a single-electron cloud(as in case muon  
 435 ionisation).

436 Such an effect indeed was observed. If we suppose a linear dependence of output signal  
 437 amplitude from number of initial electrons a relative position for experimental peak should be  
 438 located at(calibration relatively to the photopeak):

$$channel_{escapePeak} = \frac{2107.4 - 301.1}{210.42} 98 + 301.1 = 1142.3 \neq 1253.3, \quad (12)$$

439 **9 Appendix**

440 **9.1 pressure meter**

441 For the pressure measurement inside of drift tube we used pressure transmitters from  
442 SensorTechnics®. The devise is marked by ID:CTE9005AQ4, so we used appropriate datasheet  
443 from the manufacturer [5].

444 According to datasheet and marking, this pressure transmitter is designed for pressure mea-  
445 surements in the interval  $0 \dots 5 \text{ bar}$ . But on the transmitter is marked an interval  $0 \dots 3,5 \text{ bar}$ .  
446 So to be able to use this device, we additionally calibrated it.

447 For this purpose we used two control points: the output current value for atmospheric  
448 pressure at that point (727 mmHg) and a current for a vacuum. To get a vacuum we used a  
449 pump which decreases a pressure to the value  $< 0.001 \text{ bar}$  which we consider as a vacuum.

Table 5: Control points for calibration of pressure transmitter.

| pressure [bar] | voltage[V] |
|----------------|------------|
| $< 0.001$      | 0.405      |
| 1              | 0.858      |

450 Therefore the voltage dependence taken on a resistor  $100\Omega$  depends on a pressure as:

$$V = 4.05 + 0.453 \cdot P[\text{bar}] \quad (13)$$

$$P[\text{bar}] = -0.894 + 2.2075 \cdot V \quad (14)$$

451 **References**

- 452 [1] F. Hahn, F. Ambrosino, A. Ceccucci, H. Danielsson, N. Doble, F. Fantechi, A. Kluge, C.  
453 Lazzeroni, M. Lenti, G. Ruggiero, M. Sozzi, P. Valente, and R. Wanke. NA62: Technical  
454 Design Document. Technical Report NA62-10-07, CERN, Geneva
- 455 [2] SHiP Technical Proposal from 8 april 2015: arXiv:1504.04956v1
- 456 [3] GARFIELD tutorial <http://garfield.web.cern.ch/garfield>
- 457 [4] Outer Tracker calibration and open charm production cross section measurement at LHCb,  
458 2013 A.V.Kozlinskiy.  
459 <http://dspace.ubvu.vu.nl/bitstream/handle/1871/40430/dissertation.pdf>
- 460 [5] DataSheet for Pressure transmitters for corrosive liquids and gases CTE/CTU9000 series.  
461 [http://www.first-sensor.com/cms/upload/datasheets/DS\\_Standard-CTE-CTU9000\\_E\\_11509.pdf](http://www.first-sensor.com/cms/upload/datasheets/DS_Standard-CTE-CTU9000_E_11509.pdf)
- 462 [6] W. Bonivento, A. Boyarsky, H. Dijkstra, U. Egede, M. Ferro-Luzzi, B. Goddard, A. Golutvin,  
463 D. Gorbunov, R. Jacobsson, J. Panman, M. Patel, O. Ruchayskiy, T. Ruf, N.  
464 Serra, M. Shaposhnikov, and D. Treille. Proposal to Search for Heavy Neutral Leptons at  
465 the SPS. Technical Report CERN-SPSC-2013-024. SPSC-EOI-010, CERN, Geneva (Oct,  
466 2013).
- 467